Ab Initio Simulations of Phase Stability and Martensitic Transitions in NiTi

Justin B. Haskins
AMA Inc., Thermal Materials Protection Branch,
*NASA Ames Research Center, Moffett Field, California 94035, USA**

Alexander E. Thompson
*USRA, Thermal Materials Protection Branch, NASA Ames Research Center, Moffett Field, California 94035, USA**

John W. Lawson†
Thermal Materials Protection Branch, NASA Ames Research Center, Moffett Field, California 94035, USA
(Dated: August 31, 2016)

For NiTi based alloys, the shape memory effect is governed by a transition from a low-temperature martensite phase to a high-temperature austenite phase. Despite considerable experimental and computational work, basic questions regarding the stability of the phases and the martensitic phase transition remain unclear even for the simple case of binary, equiatomic NiTi. We perform *ab initio* molecular dynamics simulations to describe the temperature-dependent behavior of NiTi and resolve several of these outstanding issues. Structural correlation functions and finite temperature phonon spectra are evaluated to determine phase stability. We show that finite temperature, entropic effects stabilize the experimentally observed martensite (B19') and austenite (B2) phases while destabilizing the theoretically predicted (B33) phase. Free energy computations based on *ab initio* thermodynamic integration confirm these results and permit estimates of the transition temperature between the phases. In addition to the martensitic phase transition, we predict a new transition between the B33 and B19' phases. The role of defects in suppressing phase transformation temperatures is discussed.

I. INTRODUCTION

Shape memory alloys are materials that after deformation recover their original shape upon heating. They are technologically important for a wide range of applications, including actuators, shape-morphing wings and next generation space suits, among others. Nickel Titanium (nitinol) is perhaps the best-known example in this class of alloys and figures prominently in many commercial applications. The shape memory effect in NiTi is driven by a martensitic phase transition from a low temperature martensite phase (B19') to a high temperature austenite phase (B2).[1,2] Many applications involving shape memory alloys are tied to the specific value of the martensitic phase transition temperature.[3] Having the ability to tune this transition temperature, for example, through ternary additions in NiTi-based alloys,[3–5] will open the door to significantly more far-reaching applications. However, even for binary, equiatomic NiTi, which is the simplest example in this class of materials, basic questions regarding the stability of the phases and the martensitic phase transition remain unclear. In this paper, we resolve several of these important, outstanding issues.

Experimentally, the high temperature austenite phase of NiTi has the cubic B2 ($Pm\bar{3}m$ symmetry) structure. The low temperature martensite phase has the monoclinic B19' ($P2_1/m$ symmetry) structure, with an experimentally determined angle γ of 98°.[6,7] The transition temperature between the two phases is reported to be approximately 341 K.[8] Relevant crystal structures are shown in Fig. 1. Considerable computational work has been performed to understand the phases of NiTi and related materials. In particular, density functional theory (DFT) studies[9–22] have provided many insights into the energetics and properties of NiTi; but they have also generated new unanswered questions. For example, DFT formation energies for B2 are in good agreement with experiments[23–26]; however, B2 is predicted to be dynamically unstable at $T = 0$, i.e. certain phonons modes have imaginary frequencies.[27] Recent attempts using small systems to include finite temperatures effects into B2 stability analyses have given contradictory results.[28,29] On the other hand, B19' at the experimental monoclinic angle γ of 98° is dynamically stable at $T = 0$; however, the computed structure is unstable to shear[12]. Huang *et al.* determined the DFT ground state of NiTi at $T = 0$ to be a new orthorhombic phase (B33) with an angle of $\gamma = 107.3°$.[30] However, the B33 structure has not been observed experimentally in NiTi and its crystal symmetry ($Cmcm$) is incompatible with the shape memory effect, and therefore cannot represent the martensitic phase of this material. Thus, after considerable computational analysis, we are in the unsatisfying position that the two experimentally observed phases for NiTi have undetermined stability; whereas the only computed stable phase has never been observed and is incompatible with the shape memory effect.

To address these discrepancies, we perform high accuracy, *ab initio* molecular dynamics (AIMD) simulations based on density functional theory combined with extended thermodynamic integration methods to evaluate the stability and relative free energies for the defect-free, single crystal phases (B2, B19', B33) of NiTi for a range

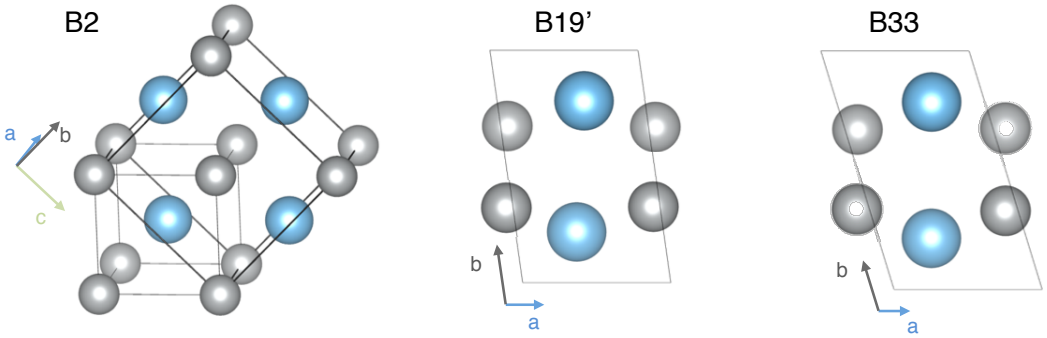

FIG. 1. Phases of NiTi including B2 in its primitive, 2 atom cell as well as in a four atom cell that is analogous to the primitive cells of B19' and B33. The monoclinic angle, γ, is defined to be between the a and b lattice vectors.

of temperatures up to 900 K. These materials are strongly anharmonic, and therefore, methods based primarily on phonon analysis, even at finite temperatures, will not capture the full behavior. This necessitates high accuracy computations of the free energy. We show that finite temperature, entropic effects resolve many of the controversies derived from previous studies, bringing computation into much closer agreement with experiment. Specifically, we show that entropic effects stabilize both B2 and B19' while destabilizing B33. Furthermore, the martensitic transition temperature is estimated between these stable phases. In addition, we also identify a new phase transition between B33 and B19'.

II. METHODS

A. Finite Temperature Optimiztion

The free energy of the B33, B19', and B2 phases were optimized with respect to lattice parameters at temperature to produce structures having negligible stress. This requires minimization of Helmholtz free energy, F, with respect to the lattice vectors, Ω. For a generalized crystal, Ω is given by

$$\Omega = \begin{bmatrix} a_x & b_x & c_x \\ a_y & b_y & c_y \\ a_z & b_z & c_z \end{bmatrix}, \tag{1}$$

where the lattice vectors are $\mathbf{a} = (a_x, a_y, a_z)$, $\mathbf{b} = (b_x, b_y, b_z)$, and $\mathbf{c} = (c_x, c_y, c_z)$.

The value of $\frac{\partial F}{\partial \Omega}$ can be written as in terms of Ω and the stress tensor, σ. The free energy of the system in the canonical ensemble is given by

$$F = -\beta^{-1}\ln(\mathcal{Z}), \tag{2}$$

where $\mathcal{Z}$ is the partition function and β^{-1} is equal to the product of the Boltzmann constant and temperature. The partition function is given by $\mathcal{Z} = \int \Pi_{i=1}^{N} d\mathbf{r}_i d\mathbf{p}_i e^{-\beta\mathcal{H}}$, where $\int \Pi_{i=1}^{N} d\mathbf{r}_i d\mathbf{p}_i ...$ represents the integral over phase space. The Hamiltonian, $\mathcal{H}$, describing this system is

$$\mathcal{H} = \sum_{i=1}^{N} \frac{\mathbf{p}_i \cdot \mathbf{p}_i}{2m_i} + U(\{\mathbf{r}_i\}), \tag{3}$$

where $\mathbf{p}_i$ and m_i are the momentum and mass of particle i, the summation in the first term is taken over the N atoms in the system, and U is potential energy, which is determined by the set of all atomic positions $\{\mathbf{r}_i\}$. The derivative of F with respect to Ω is given by

$$\frac{\partial F}{\partial \Omega} = -\beta^{-1}\frac{1}{\mathcal{Z}}\frac{\partial \mathcal{Z}}{\partial \Omega}. \tag{4}$$

One may expand the derivative of $\mathcal{Z}$ with respect to Ω by performing a canonical transformation on $\mathbf{r}$ and $\mathbf{p}$, such that

$$\begin{aligned} \mathbf{r}_i &= \Omega\boldsymbol{\rho}_i \\ \mathbf{p}_i &= \boldsymbol{\pi}_i\Omega^{-1}, \end{aligned} \tag{5}$$

where $\boldsymbol{\rho}_i$ are reduced coordinates, $\boldsymbol{\pi}_i$ are transformed momentum, and a superscript "-1" indicates the inverse tensor. This transformation preserves the dynamics derived from the Hamiltonian and leads to the partition function being written as $\int \Pi_i d\boldsymbol{\pi}_i d\boldsymbol{\rho}_i e^{-\beta\mathcal{H}(\{\boldsymbol{\pi}_i\},\{\boldsymbol{\rho}_i\})}$. The free energy expression in Eq. 4 then reduces to

$$\frac{\partial F}{\partial \Omega} = \left\langle \frac{\partial \mathcal{H}(\{\boldsymbol{\pi}_i\},\{\boldsymbol{\rho}_i\})}{\partial \Omega} \right\rangle, \tag{6}$$

where $\langle ... \rangle$ denotes the ensemble average. The transformed Hamiltonian is given by

$$\mathcal{H} = \sum_{i=1}^{N} \frac{1}{2m_i}(\boldsymbol{\pi}_i\Omega^{-1}) \cdot (\boldsymbol{\pi}_i\Omega^{-1}) + U(\{\Omega\boldsymbol{\rho}_i\}). \tag{7}$$

The derivative of $\mathcal{H}$ with respect to Ω may then be written as

$$\frac{\partial \mathcal{H}}{\partial \Omega} = \sum_{i=1}^{N} \frac{1}{m_i}(\boldsymbol{\pi}_i\Omega^{-1}) \cdot \frac{\partial(\boldsymbol{\pi}_i\Omega^{-1})}{\partial \Omega} + \sum_{i=1}^{N} \frac{\partial U}{\partial(\Omega\boldsymbol{\rho}_i)} \cdot \frac{\partial(\Omega\boldsymbol{\rho}_i)}{\partial \Omega}. \tag{8}$$

Employing vector-matrix manipulations, one may rearrange Eq. 8 as

$$\frac{\partial \mathcal{H}}{\partial \Omega} = -\sum_{i=1}^{N} \frac{1}{m}(\boldsymbol{\pi}_i \Omega^{-1}) \otimes (\boldsymbol{\pi}_i \Omega^{-1}) \Omega^{-T} - \sum_{i=1}^{N} \mathbf{f}_i \otimes \boldsymbol{\rho}_i, \quad (9)$$

where $\mathbf{f}$ is force, $\otimes$ is the outer product operation, and "$-T$" indicated the transpose of the inverse. Transforming back to $\mathbf{p}$ and $\mathbf{r}$ leads to

$$\frac{\partial \mathcal{H}}{\partial \Omega} = -\sum_{i=1}^{N} \frac{1}{m_i}(\mathbf{p}_i \otimes \mathbf{p}_i) \Omega^{-T} - \sum_{i=1}^{N} (\mathbf{f}_i \otimes \mathbf{r}_i) \Omega^{-T}. \quad (10)$$

The quantity given by $-\sum_{i=1}^{N} \{\frac{1}{m}(\mathbf{p}_i \otimes \mathbf{p}_i) + (\mathbf{f}_i \otimes \mathbf{r}_i)\}$ is the product of the absolute value of the determinant of Ω^T, or volume, with the stress tensor, $|det\Omega^T|\sigma$. Using these relations with Eq. 6 leads to the final expression for the derivative of free energy,

$$\frac{\partial F}{\partial \Omega} = |det\Omega^T|(\sigma \Omega^{-T}). \quad (11)$$

For the systems in the present work, the derivative of free energy with respect to cell was minimized iteratively. This entailed performing AIMD simulations to obtain average stresses and altering the cell according to $\Omega^{k+1} = \Omega^k - \alpha \frac{\partial F}{\partial \Omega}$, where k is an iteration index and α is a constant parameter. The stresses employed for optimization were averaged over 3 ps AIMD simulations, and a value of 2×10^{-4} was used for α. The optimization procedure was iterated until all components of the stress tensor were < 1 kbar.

B. Phonon Dispersions

Zero-temperature phonon dispersions were obtained from the frozen phonon approach using displacements of 0.01 Å. We use the Phonopy software package to plot the phonon dispersions along particular crystal directions.[31] Imaginary frequencies are indicated with negative numbers.

To obtain phonon dispersions at finite temperature, we applied the temperature dependent effective potential (TDEP) technique developed by Hellman and coworkers.[32,33] The TDEP procedure fits the elements of the force constant matrix (D_{ij}) to the forces (f_i) and displacements (u_i) generated from a MD simulation. The fit is carried out by performing a least square minimization of the difference between f_i and the force as described in the harmonic approximation.

The force as given by the harmonic approximation, $\tilde{f}_i$, is represented as

$$\tilde{f}_i = \sum_j D_{ij} u_j. \quad (12)$$

The quantity that is minimized, S, is then given by

$$S = \sum_{t,i} (f_i^t - \tilde{f}_i^t)^2, \quad (13)$$

where the summation is performed over all i atoms and t timesteps. In the present work, temperature dependent phonons were computed by fitting force data from 50 ps AIMD simulations. The force constant matrix was then symmetrized in accordance with the crystal structure.

C. Free Energy

1. Generalized Stress-Strain Method

If a transformation between two given phases can be continuously and reversibly induced *via* changes in lattice parameter, one may apply the principle of thermodynamic integration to obtain changes in Helmholtz free energy with respect to changes in the lattice vectors. When applicable, this powerful technique yields both the difference in Helmholtz free energy, ΔF, between the phases as well as the profile of ΔF as a function of lattice parameter. An important case of such a procedure has been described in detail for the case of the constant volume bcc→fcc Bain path.[34] We here generalize this formalism to treat the variable volume deformation of any cell. Incorporation of variable volume allows for a transformation path between two stable phases at a given temperature but different volumes, which is the case for the martensitic transformation.

This transformation between phases can be effected by defining Ω to be dependent on a mixing parameter, λ, that linearly changes Ω from an initial state to a final state, or $\Omega(\lambda) = \Omega^0 - \lambda(\Omega^0 - \Omega^1)$. The values of Ω at $\lambda = 0$ and 1 correspond to structures of stable phases, Ω^0 and Ω^1, respectively. Through the use of Eq. 4, the free energy change upon such a deformation may be represented as

$$\Delta F = -\beta^{-1} \int_0^1 \frac{1}{\mathcal{Z}} \frac{\partial \mathcal{Z}}{\partial \lambda} d\lambda = -\beta^{-1} \int_0^1 \frac{1}{\mathcal{Z}} \frac{\partial \mathcal{Z}}{\partial \Omega} : \frac{\partial \Omega}{\partial \lambda} d\lambda, \quad (14)$$

where $\frac{\partial \mathcal{Z}}{\partial \Omega}$ and $\frac{\partial \Omega}{\partial \lambda}$ are both tensors and ":" denotes the Frobenius inner product (*i.e.*, $\sum_{ij} \frac{\partial \mathcal{Z}}{\partial \Omega}_{ij} \frac{\partial \Omega}{\partial \lambda}_{ij}$). The free energy expression in Eq. 14 further reduces to

$$\Delta F = \int_0^1 \left\langle \frac{\partial \mathcal{H}(\boldsymbol{\pi}, \boldsymbol{\rho})}{\partial \Omega} \right\rangle : \frac{\partial \Omega}{\partial \lambda} d\lambda. \quad (15)$$

Using Eq. 10 with Eq. 15 leads to the final expression for free energy,

$$\Delta F = \int_0^1 V_\lambda \left[(\sigma \Omega^{-T}) : \frac{\partial \Omega}{\partial \lambda} \right] d\lambda, \quad (16)$$

where V_λ is defined as $|det\Omega^T|$.

In terms of NiTi, both the B33→B19' and the B19'→B2 phase transformations can be reversibly effected through changes in lattice parameter alone. The transformations as a function of Ω are furthermore continuous, as both atomic coordinates and the stress tensor

vary smoothly. The generalized stress strain technique was applied here as a function of temperature between the B33 and B19' phases as well as between the B19' and B2 phases. The integral in Eq. 16 for each phase transformation was taken over 11 values of λ, or a 0.1 spacing. The stresses needed for application of Eq. 16 were obtained from 5-10 ps AIMD simulations. Where applicable, the procedure is applied between stress free phases, which results in the difference of F between the phases being equivalent to the Gibbs free energy (G) difference.

2. Einstein Crystal Method

One may use the principles of thermodynamic integration to obtain the total free energy of a phase represented with DFT. This requires the definition of a reference crystalline phase, similar in structure to the phase as represented by DFT, with a known free energy. The free energy difference between the reference and DFT representations of the phase, $F^{\mathrm{DFT}} - F^{ref}$, is given as

$$F^{\mathrm{DFT}} - F^{ref} = \int_0^1 \left\langle \frac{\partial U}{\partial \lambda} \right\rangle_\lambda d\lambda. \tag{17}$$

The potential energy, U, is given by $U^{ref} - \lambda(U^{ref} - U^{\mathrm{DFT}})$ and the value of λ smoothly transitions the potential from U^{ref} at $\lambda = 0$ to U^{DFT} at $\lambda = 1$. The thermodynamic average of $\frac{\partial U}{\partial \lambda}$ for various values of λ may be obtained with AIMD simulations using the mixed potential.

The prototypical example of a reference system is the Einstein crystal, where atoms are anchored to fixed coordinates with a single spring constant. However, as the most desirable reference potential is one that closely approximates the DFT, the Einstein crystal, however, is a generally poor choice for U^{ref}.[34] Alternatively, one may improve the accuracy of the reference system by employing the full force constant matrix, provided the phonons are real. For NiTi, the B2 phase is unstable at 0 K, resulting in negative vibrational modes, which means the 0 K force constant matrix is not a suitable reference. To solve this problem, we employ the temperature-dependent force constant matrix as determined from AIMD simulations and the TDEP procedure previously described. Our reference system, then, takes the form

$$U^{ref} = \frac{1}{2} \sum_{i,j} u_i D_{ij} u_j, \tag{18}$$

where the displacements, u, are referenced to the temperature averaged atomic coordinates. This approach is highly accurate and allows the integration in Eq. 17 to be performed using a λ spacing of 0.25.

D. Density Functional Theory Simulations

Simulations are performed with the Vienna *Ab Initio* Simulation Package (VASP)[35–38] using the frozen core all-electron projector augmented wave method (PAW)[39,40] and the generalized gradient approximation of Perdew, Burke, and Ernzerhof.[41] All AIMD simulations employ an energy cutoff of 269.5 eV, an electronic energy convergence criteria of 1×10^{-7} eV, a time step of 3.0 fs, and ∼3000 k-points per reciprocal atom (KPPRA). Furthermore, electronic smearing is handled through the Methfessel-Paxton scheme[42] with a smearing width of 0.05 eV, and the computations are not spin polarized. For both Ni and Ti the $3d^9 4s^1$ and $3d^3 4s^1$ electrons, respectively, are included in the valence. This valence configuration was found to produce free energy results within 1 meV/atom agreement with simulations employing smaller cores that include the $3p^6$ electrons in the Ni and Ti valences. Computations are performed on 144 atom supercells, using the four atom unit cell, which were found to be free of vibrational size effects. Temperature is controlled through the use of a Langevin thermostat with a simulation-time equivalent friction factor of 100 fs.

III. RESULTS

A. Convergence Tests

To ensure the accuracy of our simulations, we have performed a thorough set of tests to ensure our results are converged with respect to numerical accuracy, the number of valence electrons, and simulation size. For numerical accuracy, we consider the convergence of the 0 K energetics and finite temperature free energetics with respect to increasing KPPRA and E_c. A similar approach is taken to asses the impact of the valence configuration on the accuracy of the simulation; the number of valence electrons is increased unit both energy and free energy converge. Finally, simulation size effects are evaluated largely on the basis of vibrational convergence, which is quantified through the finite temperature phonon dispersion.

In terms of numerical accuracy, we consider convergence with respect to the number of KPPRA and the value of E_c, though energetic convergence with respect to additional factors is examined in the Supplementary information (Tables S1 and S2 and Figs. S1-S3). In particular, convergence of the 0 K energy difference between B2 and B19' is provided in Fig. S1 of the Supplementary information. The least accurate configuration in Fig. S1 corresponds to the typical AIMD configuration in this work, with ∼3000 KPPRA and E_c = 268.5 eV. We see that increasing the number of KPPRA from 3000 to 42000 leads to a 1 meV/atom increase in the energy between the B2 and B19' structures. Conversely, increasing E_c up to 700 eV leads to only a slight decrease in energy

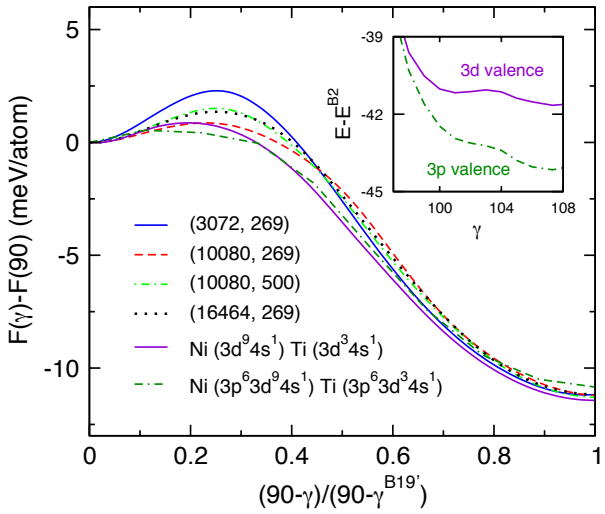

FIG. 2. Free energy as a function of normalized monoclinic angle $(90\text{-}\gamma)/(90\text{-}\gamma^{B19'})$ between B2 and B19' as determined by the stress-strain method for various levels of numerical accuracy, given in brackets as (KPPRA,E_c) and different valence configurations. The default configuration is a 3x2x2 supercell using the 4-atom unit cell representation (48 atoms), the $3d^8 4s^2$ valence for Ni and the $3p^6 3d^2 4s^2$ valence for Ti, a plane-wave energy cutoff of 269.5 eV, and 10080 KPPRA. Zero temperature energetics as a function of γ are given in the inset as a function of valence configuration.

between the B2 and B19' phases.

To understand how the numerical accuracy of simulations affect free energy, we have applied the generalized stress-strain method to understand the free energy difference between the B19' and B2 phase using a small 3x2x2 supercell composed of 4 atom unit cells (48 atoms) at 300 K. The free energy profiles, given in Fig. 2, show that varying the number of KPPRA from 3072 to 16464 and E_c from 269.5 to 500 eV leads to a negligible change in the free energy difference between B2 and B19'. The profile, in particular the barrier, is more sensitive to these changes and varies by up to 2 meV/atom range depending on accuracy. Our results suggest entropic effects dilute the impact of 0 K energetic accuracy on free energy.

The influence of different valence configurations on the energetics as a function of normalized γ (90^o and 107.3^o correspond to B2 and B33) are shown in Fig. S2 of the Supplementary information. The smallest valence considered in Fig. S2 is the $3d^8 4s^2$ for Ni and the $3d^2 4s^2$ for Ti, while the largest is the $3p^6 3d^8 4s^2$ for Ni and $3s^2 3p^6 3d^2 4s^2$ for Ti. One may note the oscillatory approach to convergence, where adding the 3p electrons to the Ni valence leads to a 3.7 meV/atom decrease at B33, which is attenuated by increasing number of Ti valence electrons. The energy of B33 using the smallest valence deviates from that of the largest valence by 2.4 meV/atom. It appears that the systems are converged with respect to the Ti valence, where the additional 3s electrons do not further alter the energy. Though PAW potentials for Ni having the 3s electrons in the valence are not available, it is unlikely that deeper electron states will significantly alter the energetics. The smallest valence is also differentiated from the others in that it yields a stable B19' phase while the others yield no energy minima aside from B33. This result parallels the calculations shown in the Supplementary information (Table S1), where potentials with small valences are shown to produce phases that are not stable when calculated with larger valences.

The largest valences are not computationally tenable to long and large AIMD simulations at present, which has led us to employ the smallest valence configuration. To understand the influence of this choice of valence on free energy, we show the free energy profile as obtained from our small 48 atom supercell between the B2 and B19' as a function of normalized γ for different valence configurations at 300 K in Fig 2. Three valence configurations were tested, the smallest configuration, one having the 3p electrons of Ti and one having the 3p electrons of both Ni and Ti. As with our assessment of numerical accuracy, we again find only minor differences in the free energy of the B2 and B19' phases. The major difference in the profile occur for intermediate interpolated cells, which vary in free energy by up to 2.5 meV/atom at a given value of γ.

The primary outcome of the numerical and valence size tolerance test is that errors in 0 K energetics do not correlate, necessarily, to errors in temperature dependent free energies. In fact, the free energies appear to be relatively insensitive to all tested changes in numerical accuracy. To investigate the origin of this, we have evaluated the value of ΔE for the B2 and B19' phases employed to generate the free energy curves in Figs. 2. We have found for all cases that ΔE varies by less than 1 meV/atom for each numerical or valence configuration. It appears, then, that anharmonic effects, which lead to deviations in average potential energy away from that expected at 0 K, drive simulations at different levels of accuracy to similar energetic and entropic states.

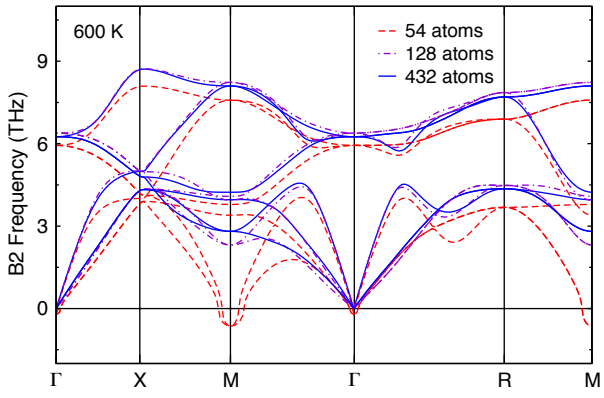

FIG. 3. Temperature-dependent phonon dispersions of 3x3x3 (54 atoms), 4x4x4 (128 atoms), and 6x6x6 (432 atoms) supercells of B2 at 600 K.

The noted anharmonic effects are largely a product of vibrational (phonon) structure and scattering. It is thereby necessary to ensure that such effects are sufficiently converged with respect to system size. For AIMD simulations using small systems with periodic boundaries, anomalous phonon self-interactions can dramatically alter the nature of anharmonic effects on the system. To begin, an evaluation of the dependence of the phonon dispersion with respect to supercell size configuration at 0 K was performed for all phases, as given in Figs. S4-S6 of the Supplementary material. The resulting phonon dispersions are relatively insensitive to supercell size, though the B2 acoustic modes near Γ show slight sensitivity along the M→ Γ direction. The vibrational modes of B33 and B19' are real, indicating that the phases are stable at 0 K. On the other hand, the TA mode of B2 exhibits several imaginary (given as negative) frequencies both at M and along the Γ →R→X direction. To examine the influence of size dependent anharmonic effects on B2, we perform a limited set of AIMD simulations on the 3x3x3 (54 atoms), 4x4x4 (128 atoms), and 6x6x6 (432 atoms) supercells of B2 at 600 K and use the TDEP approach to characterize the vibrations, as given in Fig. 3. At the 54 atom size, the imaginary modes centered on the M-point are present, indicating instability. For the larger 128 and 432 atom cells, the imaginary modes are not present, and the B2 phase appears to be stable. We therefore use systems similar in size to the 128 atom cell for our AIMD simulations to avoid error in the vibrational dispersion. For the 4 atom unit cell employed in most of the present work, this corresponds to a 4x3x3, or 144 atom, supercell, which is employed in the majority of this work. Simulations using this supercell size are computational tractable and provide vibrational accuracy comparable to larger supercell.

B. Phase Stability

For B2, B19', and B33, we consider phase stability from several complementary viewpoints. For each case, the lattice vectors of the AIMD simulation cells are optimized such that all finite temperature components of the stress tensor are zero. This procedure not only accounts for thermal expansion, but also places the system at a critical point on the free energy surface, implying elastic stability. We also examine deviations of the crystalline structure from ideality during the course of the simulations in these optimized cells. Structural evolution is evaluated quantitatively with: (1) normalized position correlation functions (NPCFs) [43] and (2) atomic displacement scatter diagrams.[44] The NPCF is proportional to $\sum_i \langle (r_i(t-t_0) - R_i^0) \cdot (r_i(t_0) - R_i^0) \rangle$ where $r_i(t)$ are the atomic trajectories from the AIMD simulation, R_i^0 is the ideal reference lattice vectors of interest and the brackets are ensemble averages. For long times ($t \to \infty$), vibrational motion becomes uncorrelated, and therefore, NPCF $\to 0$ indicates stabilization with respect to the reference lattice whereas nonzero values indicate the converse. Atomic displacements are plotted relative to the reference structures on scatter diagrams. Significant deviations from zero displacement signal an instability. Finally, the temperature dependent phonon dispersions are computed using the TDEP method. The presence of imaginary modes indicate instability.

Concerning the temperature dependent structure optimization, the value of γ for B19' and B33 is allowed to change to produce negligible shear stress, while γ is held 90° for B2. The value of γ is sensitive to temperature for B19', while it remained near 107.3° for B33. Barrierless, and spontaneous, B33→B19' and B19'→B2 transitions were found upon optimization at critical temperatures of 400 K and 800 K, respectively, which represent upper temperature bounds to stability. For simulations on these phases at and above the critical temperature, geometry optimization was performed with γ for B33 and B19' being held to the terminal values of 107.32° and 97°, respectively.

Both NPCFs as well as atomic displacement scatter plots are shown in Fig. 4 for 144 atom cells of B33, B19', and B2. Fig. 4a, b, and c, shows very different behavior for the three phase at different temperatures. For B33, the NPCFs indicate structural stability at lower temperatures, 50 K and 300 K, but instability for $T > 300$ K. Convergence times at 300 K are almost two orders of magnitude larger than at 50 K. This may indicate the proximity of a stability transition for B33. Interestingly, the B19' phase loses its $T = 0$ non-zero shear stress even at low T and maintains its ideal configuration up to 700 K. Perhaps most striking is that while the B2 structure is unstable at 50 K, it stabilizes for $T \geq 300$ K. Unlike B33, the NPCF convergence rates for B2 increase with increasing temperature.

The atomic displacements scatter plots for B2, B19', and B33 are shown in the overlay plots in Fig. 4a, b, and c, respectively. For each case, displacements are provided for 50 K (blue circles) and 600 K (red squares). At low temperatures, B33 displacements are negligible; however, at high temperatures, large displacements on the order of 0.5 Å can be seen in the a direction. Displacements in a result from thermally induced motion along the [100](011) stacking fault, which previously has been shown from DFT calculations to be important for the martensitic transition.[9,10] At low and high temperatures, the B19' phase exhibits only minor displacements, ~ 0.05 Å. The B19' displacements do not show any particular ordering and can most likely be attributed to vibrational motion, as indicated by the loss of correlation in the NPCF. The B2 phase at low temperatures shows large displacements ~ 0.4 Å from ideality. At higher temperatures, however, these displacements largely vanish, as seen in the tight clustering near the origin. Both the NPCF and the atomic scatter plots indicate that for $T > 300$ K, the high temperature phase of NiTi is very closely approximated by ideal B2.

Phase stability is further investigated by explicit

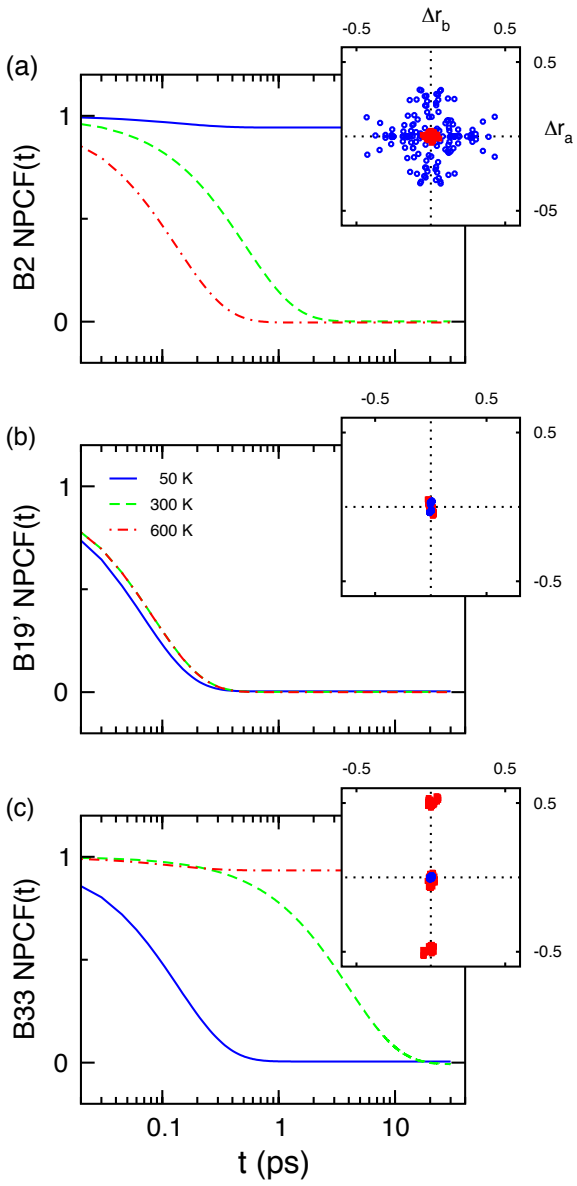

FIG. 4. Normalized position correlation function (NPCF) and scatter plots of average atomic displacements from ideal positions along the a (Δr_a) and b (Δr_b) lattice vectors for (a) B2, (b) B19', and (c) B33. The NPCFs are given for the 144 supercell at 50, 300, and 600 K and differentiate between stable (NPCF(∞) $\sim$ 0) and unstable (NPCF(∞) $\sim$ 1) structures. For all cells, scatter plots are given for the lowest tested temperature of 50 K (blue circles) and 600 K (red squares).

computation of temperature-dependent phonons as derived from the AIMD simulations.[32,33] Imaginary phonon modes (represented as negative numbers) indicate the crystal structure is dynamically unstable, i.e. it is not a local minima of the energy. Phonon spectra are shown in Fig. 5 at both zero-temperature and at 600 K. It is important to note that these results are very sensitive to cell size, and as mentioned before, using sufficiently large cells is crucial to obtain reliable results. The B33 phase, given in Fig. 5a, develops imaginary modes at 600 K through the lowering of the TA mode along the $\Gamma \rightarrow A$ direction. The presence of imaginary frequencies for long wavelength modes indicates loss of elastic stability, which drives B33→B19'. Phonon dispersions for the B19' phase show stability across the full temperature range investigated, as given in Fig. 5b. Most dramatically perhaps, the imaginary modes reported for the B2 $T = 0$ K phonon dispersion lift and become positive at 300 K, as shown in Fig. 5a, indicating stabilization of this phase, consistent with the structure analysis of Fig. 4.

The stress tensor, structure, and phonon analyses provide a complementary picture of the temperature dependent stability of the three phases that is consistent with experiment. Namely, stable phases at a given temperature exhibit the following properties: all components of the stress tensor (normal stresses and shears) are on average zero; the NPCF goes to zero in finite time; and all phonon modes are positive. Though shown for a representative set of temperatures here, these analysis were performed for all cells between 50 K and 900 K is regular intervals of 50 K. Our results along the entire temperature range show that finite temperature, anharmonic effects stabilize the high-temperature B2 phase at and above 300 K. The low-temperature B33 phase is progressively destabilized, fully losing stability near 200 K. The B19' phase, on the other hand, is unstable to shear at $T = 0$ but exhibits full stability from 50 K up to 700 K.

C. Free Energy Computations

To obtain further insights into phase stability as well as transitions between the phases, we compute the relative free energies of the phases. Vibrational entropy is frequently evaluated via the quasi-harmonic approximation (QHA). However, stability issues at $T = 0$ invalidates this approach for B2 due to the appearance of imaginary phonon modes. Alternatively, stable, finite temperature phonon spectra can be used with the QHA expressions to obtain entropy estimates. However, for strongly anharmonic phases, such as B2 NiTi, this approach is not expected to be a good approximation to the full anharmonic free energy. Strongly anharmonic systems warrant the use of high accuracy methods for computing free energies. For this reason, we use two different methods based on thermodynamic integration to compute the free energies.

Our first approach is a generalization of the stress-strain methods developed previously for transition metals.[34] Those methods based on Bain path integration are necessarily volume conserving; however, many systems of interest including NiTi do not conserve volume between the phases. As previously described, we generalized that approach to account for arbitrary cell and volume changes in an exact way. Our generalized stress-strain method requires a well defined, continuous path in lattice vector space between the two given phases. For

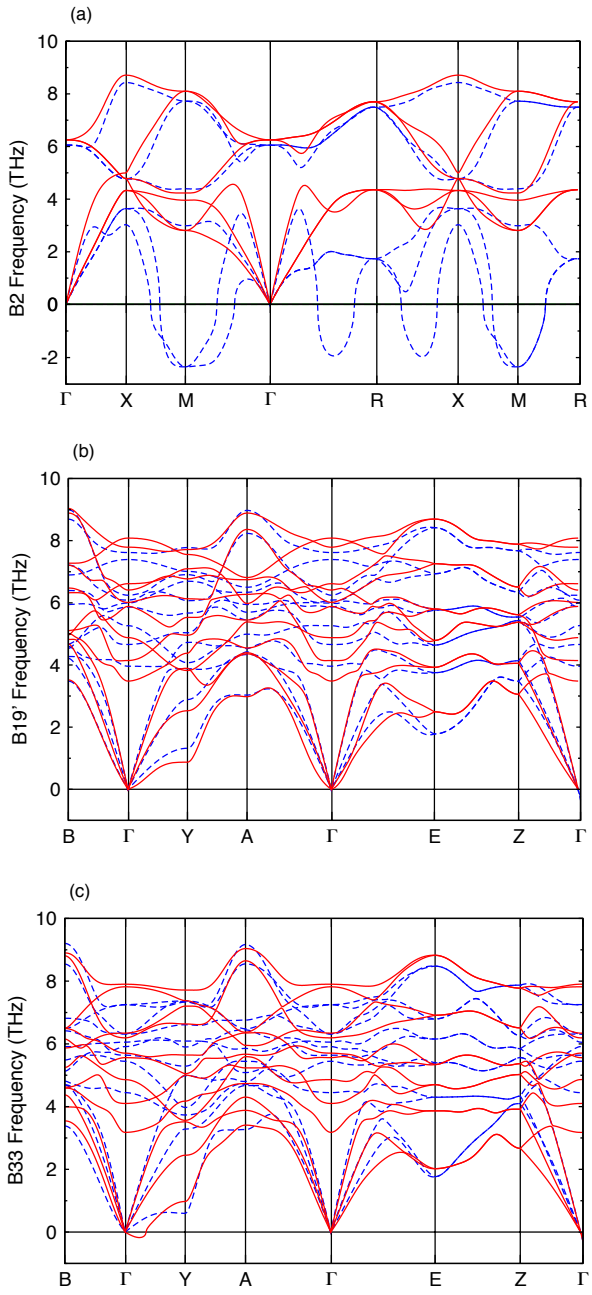

FIG. 5. Phonons of the (a) B2, (b) B19', and (c) B33 phases of NiTi at 0 K (blue, dashed line) and 600 K (red, solid line). Temperature-dependent phonons are extracted from simulations using the 144 atom supercell.

NiTi, the monoclinic angle, γ, provides a natural, continuous parameter to connect the three phases of interest shown in Fig. 1. In general, multiple paths can be considered; however, the B33→B19'→B2 path was determined to be the best behaved and is equivalent to motion along the $\langle 100 \rangle \{110\}$ generalized stacking faults. Spontaneous motion along this fault was found in the high temperature B33 phase during structural stability tests. The B33→B19' path is largely a transformation in γ-space, as the lattice vectors are of comparable magnitude, while the B19'→B2 path involves non-trivial changes to both γ as well as the lattice vectors. Optimization of the simulation cells to obtain zero stress is required to ensure the obtained free energy differences, which are Helmholtz free energy differences, are equivalent to Gibbs free energy differences. We find the internal atomic coordinates for the 144 atom cell for this path to transform continuously and that the stresses converge rapidly (< 10 ps) (see Supplemental Fig. S7). It should be noted that while free energy differences between stable phases can be rigorously computed, evaluation of free energies differences involving unstable structures is still an area of active investigation. Therefore, free energies involving unstable structures may contain some systematic error as discussed recently.[45]

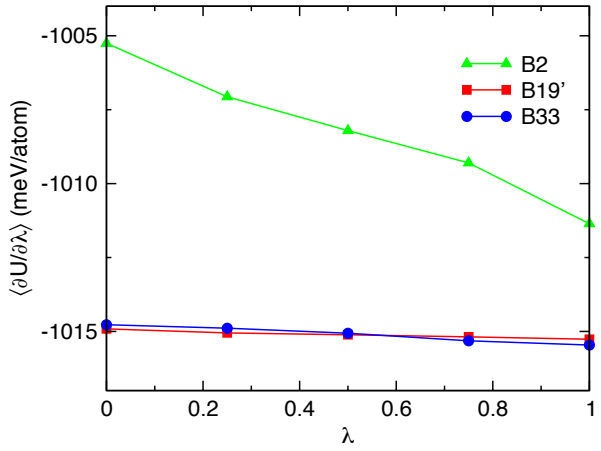

FIG. 6. Profile of $\langle \partial U/\partial \lambda \rangle$ at 300 K as a function of λ for B2, B19', and B33. Results are shown for 300 K and a 4x3x3, 144 atom supercell. Larger differences between derivative values at $\lambda = 0$ and 1 signify more anharmonic character.

Our second approach uses the Einstein crystal method to compute free energy differences at isolated points along the transformation paths. These computations were used to check the stress-strain method and were only performed at free energy mimina along the transformation path. The reference harmonic free energy is obtained from the force constants associated with the temperature dependent phonon dispersions. This approach overcomes difficulties in using $T = 0$ K phonon dispersions with imaginary modes. For each stable crystal at a given temperature, thermodynamic integration is performed from the system described by the harmonic reference potential to the one described by DFT.

A representation of the integrand for the Einstein crystal appoach, $\langle \partial U/\partial \lambda \rangle$, as a function of the potential energy mixing parameter, λ, is provided in Fig. 6 for all phases at 300 K. The highly harmonic nature of B33 and B19' are reflected in the minor variation in $\partial U/\partial \lambda$ over the λ range, suggesting the largest correction to the quasiharmonic free energy is a constant factor originat-

ing from potential energy shifts. The large variation of $\partial U/\partial\lambda$ for B2, on the other hand, may be attributed to its highly anharmonic character. We find that the anharmonic contributions to the free energy of B2 to be on the order of $3-5$ meV/atom compared to the harmonic reference free energy. This nontrivial anharmonic contribution to the free energy can shift the transition temperature by as much as 100 K and thus confirms the need for high accuracy or exact methods to study these systems.

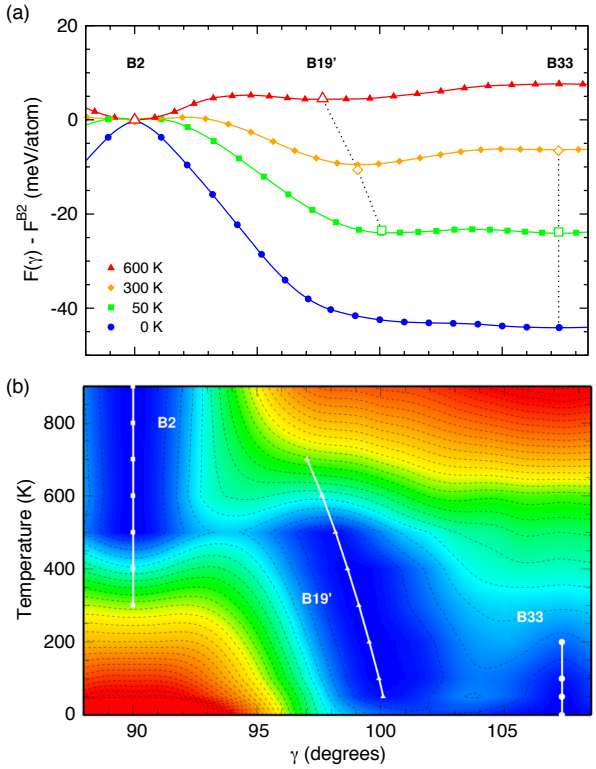

FIG. 7. Helmholtz free energy along the γ reaction coordinate as a function of temperature. (a) The free energy profile along the γ reaction coordinate for 0, 50, 300, and 600 K. Filled symbols and lines are obtained through the generalized stress-strain method, while open symbols are provided for free energy minima using the Einstein crystal approach. Error bars for the Einstein crystal method are < 1 meV/atom and not visible at the present scale. (b) Free energy color map as a function of temperature and γ. Regions of low free energy are given as blue, while regions of high free energy are given as red. White lines describe stability basins and also indicates the temperature dependence for the B19' monoclinic angle.

Free energy results using the generalized stress-strain method at 0, 50, 300, and 600 K are given in Fig. 7a as a function of γ. Einstein crystal results are shown as open symbols. Agreement between the methods is excellent (≤ 1 meV/atom). The $T = 0$ curve reproduces previous DFT results, and clearly shows that B2 and B19' are not energetic minima whereas B33 is a stable minimum, as reported by Huang *et al.*[30] We see that the free energy surface changes considerably as a function of temperature. Between B33 and B19', a small but distinguishable barrier develops between the phases for $T = 50K-300K$. Above 600 K, however, the free energy is monotonically decreasing from B33 to B19'. Importantly, B19' develops a clearly defined free energy minima above 50 K. Thus, B19' is entropically stabilized and develops into a separate phase distinct from B33. The B2 phase is unstable to transitions to B19' until 300 K, above which a free energy barrier develops stabilizing this phase as a local minima. These results are consistent with the structural and phonon analysis.

Further detail is provided by Fig. 7b where free energy differences relative to the most stable phase are mapped as a function of T and γ. Blue and red represent small and large free energy differences, respectively. The free energies are again derived from the generalized stress-strain method. The free energy map illustrates the stability regions associated with each of the phases: B33, B19', and B2. White circles indicate stable points of each phase, i.e. all finite temperature stresses are zero and all finite temperature phonons are real and positive. Thus each white circle represents a stable, free energy miminum for that phase and the white lines denote the extent of the stable free energy basins. Free energy and stability results are provided for 50 K as well as between 0 and 900 K in steps of 100 K. The regions of stability for each phase are found to be $0 < T < 200$ K for B33, $50 < T < 700$ K for B19', and $T \geq 300$ K for B2. Interestingly, the B19' angle is shown to be a function of temperature, ranging from $\sim 100^\circ$ at 50 K to $\sim 98^\circ$ at 600 K. Furthermore, the stable basin of B19' is relatively shallow suggesting that γ values for this phase might be fairly sensitive to small changes in stress. This could be important as stress fields associated with defects could potentially alter the value of γ quoted here. The free energy results allow us to estimate the phase transition temperatures. In particular from Fig. 7, the transition between B33 and B19' clearly occurs between 50 and 300 K. The B19'→B2 free energy path is uphill until 600 K, indicating that a transition occurs between 300 and 600 K.

Differences in the Gibb's free energy (ΔG) between the various stable phases as a function of T are plotted in Fig. 8. A free energy difference of zero indicates the phase transition temperature. For the B33 to B19' transition, ΔG becomes zero at 75±26 K. For B19' to B2, ΔG goes to zero at 500±14 K. The larger error for the low-T transition is a function of the slope of ΔG and the target accuracy of 1 meV/atom. The low values for the B33→B19' transition temperature explains the lack of experimental evidence for B33, despite being energetically favored at 0 K. If B33 becomes unstable at low temperatures, it may be difficult to synthesize and, therefore, to observe. The B19'→B2 transition temperature is roughly 150 K above the experimental value of 341 K.[8] However, the methods used to obtain this value, based on *ab initio* thermodynamic integration, are numerically exact to within the accuracy of DFT. There-

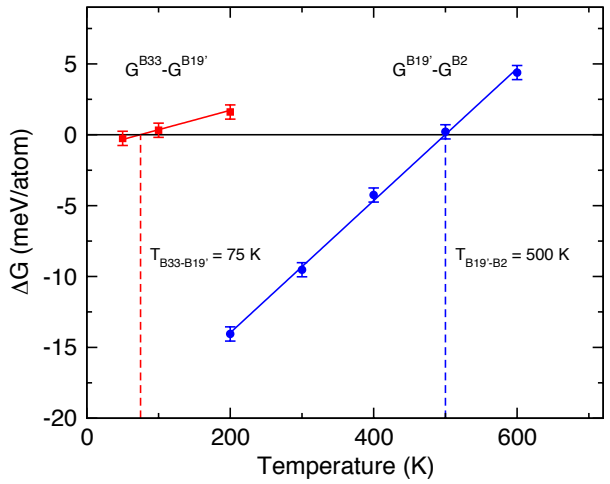

FIG. 8. Gibbs free energy differences between B33 and B19' (squares) as well as between B19' and B2 (circles) phases as a function of temperature. Interpolated transition temperatures are indicated with dashed lines. Error bars reflect the 1 meV/atom accuracy of the computations.

fore, we expect it to be a reliable estimate of the martensitic transition temperature for defect-free, single crystal NiTi. The non-trivial difference with experimental values is most likely due to defects that have been shown to suppress transition temperatures in this and related materials.[46] This also suggests that improved processing resulting in higher material quality could produce materials with higher measured transition temperatures. In addition, it is also known that the transition temperature is dependent on the heating and cooling rates with slower rates giving higher transition temperatures. As we use equilibrium methods to estimate this temperature, our results correspond effectively to infinitely slow rates. For that reason, we expect them to be an upper bound for the experimental transition temperature.

IV. CONCLUSIONS

We have performed a comprehensive computational analysis based on *ab initio* molecular dynamics of the stability and transitions between the major phases of NiTi: B2, B19', and B33. Considerable previous computational analysis based mainly on $T = 0$ DFT resulted in significant discrepancies between experiment and computation. We have shown that by including temperature dependent entropic effects into the computations, many of these differences can be resolved. We show that B2 and B19' are stabilized due to these entropic effects, whereas B33 is destabilized. These materials are shown to be highly anharmonic. Anharmonic contributions to the free energy can shift the transition temperature by as much as 100K and thus necessitates the need for high accuracy or exact methods to study these systems. We develop a generalized stress-strain method to perform such computations. The phase transition temperature between B2 and B19' is computed to be approximately 500 K for defect-free, single crystals which is about 150 K above experimental results. Defects and non-equilibrium rate effects are expected to suppress the transition temperature and bring it more into line with experiments.[46] This also suggests opportunities to obtain higher transition temperatures with current materials by improved material processing. A new phase transition in this material is identified between B33 and B19' at a computed transition temperature of 75 K. High temperature destabilization of B33 and the corresponding low transition temperature to B19' could explain why B33 has not yet been observed experimentally. Defects could affect this transition as well.

ACKNOWLEDGMENTS

This work was supported by funding from the NASA Aeronautics Research Mission Directorate's Transformational Tools & Technologies (TTT) project. We benefited from discussions with Charles Bauschlicher, Ronald Noebe, and Othmane Benafan.

* Contributed equally to this work
† john.w.lawson@nasa.gov

[1] J. A. Shaw and S. Kyriakides, J. Mech. Phys. Solids **43**, 1243 (1995).
[2] O. Benafan, S. A. Padula, R. D. Noebe, T. Sisneros, and R. Vaidyanathan, J. Appl. Phys. **112**, 093510 (2012).
[3] J. Ma, I. Karaman, and R. D. Noebe, Int. Mater. Rev. **55**, 257 (2013).
[4] R. Zarnetta, R. Takahashi, M. L. Young, A. Savan, Y. Furuya, S. Thienhaus, Maaß, M. Rahim, J. Frenzel, H. Brunken, Y. S. Chu, V. Srivastava, R. D. James, I. Takeuchi, G. Eggeler, and A. Ludwig, Adv. Funct. Mater. **20**, 1917 (2010).
[5] A. N. Bucsek, G. A. Hudish, G. S. Bigelow, R. D. Noebe, and A. P. Stebner, Shap. Mem. Superelasticity **2**, 62 (2016).
[6] G. M. Michal and R. Sinclair, Acta Crystallogr. B **37**, 1803 (1981).
[7] W. Brüher, R. Gotthardt, A. Kulik, O. Mercier, and F. Staub, J. Phys. F. **13**, L77 (1983).
[8] S. D. Prokishkin, Acta Mater. **52**, 4479 (2004).
[9] N. Hatcher, O. Y. Kontsevoi, and A. J. Freeman, Phys. Rev. B **79**, 020202 (2009).
[10] N. Hatcher, O. Y. Kontsevoi, and A. J. Freeman, Phys. Rev. B **80**, 144203 (2009).
[11] G. Vishnu and A. Strachan, Phys. Rev. B **85**, 014114 (2012).

[12] M. F.-X. Wagner and W. Windl, Acta Mater. **56**, 6232 (2008).
[13] J. Wang and H. Sehitoglu, Appl. Phys. Lett. **101**, 081907 (2012).
[14] X. Huang, C. Bungaro, V. Godlevsky, and K. M. Rabe, Phys. Rev. B **65**, 014108 (2001).
[15] D. Holec, M. Friák, A. Dlouhý, and J. Neugebauer, Phys. Rev. B **84**, 224119 (2011).
[16] S. Kibey, H. Sehitoglu, and D. Johnson, Acta Mater. **57**, 1624 (2009).
[17] P. Šesták, M. Černý, and J. Pokluda, Comput. Mater. Sci. **87**, 107 (2014).
[18] A. Pasturel, C. Colinet, D. Manh, A. Paxton, and M. van Schilfgaarde, Phys. Rev. B **52**, 15176 (1995).
[19] X.-Q. Wang, Phys. Rev. B **78**, 092103 (2008).
[20] Y. Ye, C. Chan, and K. Ho, Phys. Rev. B **56**, 3678 (1997).
[21] Z.-Y. Zeng, C.-E. Hu, L.-C. Cai, X.-R. Chen, and F.-Q. Jing, J. Appl. Phys. **109**, 043503 (2011).
[22] P. Šesták, M. Černý, and J. Pokluda, Intermetallics **19**, 1567 (2011).
[23] R. Hu, P. Nash, and Q. Chen, J. Phase Equilibria Diffus. **30**, 559 (2009).
[24] O. Kubaschewski, Trans. Faraday Soc. Engl. **54**, 814 (1958).
[25] J. Gachon, M. Notin, and J. Hertz, Thermochim. Acta **48**, 155 (1981).
[26] Q. Guo and O. Kleppa, J. Alloys Compd. **269**, 181 (1998).
[27] K. Parlinski and M. Parlinska-Wojtan, Phys. Rev. B **66**, 064307 (2002).
[28] P. Sourvatzis, D. Legut, O. Eriksson, and M. Katsnelson, Phys. Rev. B **81**, 092201 (2010).
[29] N. A. Zarkevich and D. D. Johnson, Phys. Rev. B **90**, 060102 (2014).
[30] X. Huang, G. J. Ackland, and K. M. Rabe, Nature Mater. **2**, 307 (2003).
[31] A. Togo, F. Oba, and I. Tanaka, Phys. Rev. B **78**, 134106 (2008).
[32] O. Hellman, I. A. Abriksosov, and S. I. Simak, Phys. Rev. B **84**, 180301 (2011).
[33] O. Hellman, I. A. Abriksosov, and S. I. Simak, Phys. Rev. B **87**, 104111 (2013).
[34] C. Carzola, D. Alfé, and M. J. Gillan, Phys. Rev. B **85**, 064113 (2012).
[35] G. Kresse and J. Hafner, Phys. Rev. B **47**, 558 (1993).
[36] G. Kresse and J. Hafner, Phys. Rev. B **49**, 14251 (1994).
[37] G. Kresse and J. Furthmüller, Comput. Mat. Sci. **6**, 15 (1996).
[38] G. Kresse and J. Furthmüller, Phys. Rev. B **54**, 11169 (1996).
[39] P. E. Blochl, Phys. Rev. B **50**, 17953 (1994).
[40] G. Kresse and D. Joubert, Phys. Rev. B **59**, 1758 (1999).
[41] J. P. Perdew, K. Burke, and M. Ernzerhof, Phys. Rev. Lett. **77**, 3865 (1996).
[42] M. Methfessel and A. T. Paxton, Phys. Rev. Lett. **78**, 1396 (1997).
[43] L. Vocadlo, D. Alfé, M. Gillan, I. Wood, J. Brodholt, and G. David Price, Nature **31**, 536 (2003).
[44] C. Asker, A. Belonoshko, A. Mikhaylushkin, and I. Abrikosov, Phys. Rev. B **77**, 220102(R) (2008).
[45] A. van de Walle, Q. Hong, S. Kadkhodaei, and R. Sun, Nat. Commun. **6**, 7559 (2015).
[46] A. Tehrani, H. Shahrokhshahi, N. Parvin, and J. Brgoch, J. Appl. Phys. **118**, 014901 (2015).